激光与光电子学进展

Phosphate-Bismuthate Glass and Fiber with Heavy Doping of Silver Nanoparticles (Invited)

Chen Fuguang[1†], Jiang Bofan[2†], Chen Zhi[1], Ma Siyuan[1*], Huang Yupeng[2], Zhang Hang[3**], Ma Zhijun[1***]

[1]*Research Center for Humanoid Sensing, Zhejiang Lab, Hangzhou* 311121, *Zhejiang, China*;

[2]*State Key Laboratory of Luminescent Materials and Devices, School of Materials Science and Engineering, South China University of Technology, Guangzhou* 510641, *Guangdong, China*;

[3]*Laboratory for Shock Wave and Detonation Physics Research, Institute of Fluid Physics, China Academy of Engineering Physics, Mianyang* 621900, *Sichuan, China*

Abstract Glass with heavy doping of noble metal nanoparticles is expected to exhibit high optical nonlinearity. In this study, the effects of glass composition, structure, and heat treatment on the formation of silver nanoparticles (Ag NPs) in phosphate-bismuthate (PB) glass are investigated. By optimizing the chemical composition and preparation parameters, strong localized surface plasmon resonance is achieved in the PB glass with a silver mass fraction of more than 13%, which is 20 and 6 times higher than that in bismuthate and phosphate glasses reported previously, respectively. The high solubility of the phosphate component and the self-reduction effect of the bismuthate component jointly contributed to the stability and high content of Ag NPs in the PB glass. Z-scan measurements show that such heavy doping PB glass has a reverse saturable absorption coefficient of -14×10^{-12} m·W^{-1} and a saturable absorption coefficient of 4.94×10^{-12} m·W^{-1} at 800 nm. Furthermore, the heavy doping PB glass exhibits excellent thermal stability, making it promising for the fabrication of nonlinear optical fibers. In addition, with a heavily silver-doped PB glass rod as the core and a commercial silicate glass tube as the cladding, a composite glass fiber with high Ag-NP doping is successfully fabricated using a "molten-core" fiber drawing method.

Key words phosphate-bismuthate glass; silver nanoparticle; optical nonlinearity; molten-core fiber drawing

中图分类号 TN253 **文献标志码** A **DOI**: 10.3788/LOP232216

1 Introduction

Nonlinear optical (NLO) devices, as imperative light-to-light modulators, have attracted considerable research attention owing to their potential application in various fields, including ultrafast lasers, optical limiting, and optical switches[1-15]. In recent years, noble metal nanoparticles (NPs), two-dimensional materials, semiconductor quantum dots, and carbon nanotubes have been extensively investigated because of their excellent NLO performance [5-7]. However, most of the aforementioned materials lack practicality because of their poor stability and complex preparation processes. Moreover, the tiny space sizes of the materials result in short light-matter interaction lengths, reducing the NLO performance[8-13]. Therefore, the development of other NLO materials that can be conveniently and economically fabricated and effectively extend the light-matter interaction length is still being pursued.

Inorganic glasses have opened a new path for NLO materials because they have excellent stability and can be processed into ultrafine fibers via thermal drawing, which can effectively extend the light-matter interaction length, thereby providing high convenience in device integration. However, the NLO properties of different glasses vary considerably. The nonlinear index of

收稿日期: 2023-09-28; **修回日期**: 2023-10-30; **录用日期**: 2023-11-07; **网络首发日期**: 2023-11-17

基金项目: 国家自然科学基金(62375246,U20A20211,62105297)、国家重点研发计划(2021YFB2800500)、浙江省自然科学基金(LQ22A040011,LZ23F050002)

通信作者: *masy@zhejianglab.com; **zhanghang@caep.cn; ***zhijma@zhejianglab.com

†共同第一作者

refraction (n_2) at a wavelength of 1500 nm for silica glass is only ~2.5×10^{-20} m^2/W. Consequently, considerably long fibers are required to achieve satisfactory NLO performance. In 2016, Qiao *et al.* [16] reported that n_2 at 3–3.5 μm wavelengths for $Ge_{20}Sn_xSe_{80-x}$ glass increased to 8.09×10^{-18} m^2/W and 1.41×10^{-18} m^2/W, respectively. However, the nonlinear performance of chalcogenide glass in the working band considerably decreases because of the presence of —OH, which increases the preparation difficulty. In 2017, Qiu *et al.* [17] reported a novel halide glass system Ga_2S_3-Sb_2S_3-CsI; the value of n_2 at a 1.5 μm wavelength was ($1.7-8.7$) $\times10^{-14}$ m^2/W. However, halide glass exhibits poor chemical stability and cannot be used in various environments. Alternatively, compared with the aforementioned glasses, bismuthate glass is not only chemically stable but also has a nonlinear index of refraction as high as 1.8×10^{-17} m^2/W. In 1999, Sugimoto *et al.* [18] reported that the third-order nonlinear susceptibility ($\chi^{(3)}$) of bismuthate glass was up to 9.3×10^{-12} esu (1 C=3×10^9 esu), which was close to that of As_2S_3 glass (1.1×10^{-11} esu). However, the nonlinear properties of glass fibers are considerably inferior to those of noble metal NPs (10^{-7} esu) [19-20], which limits their practical application. Therefore, the key problem of enhancing the nonlinear properties of glass fibers remains unsolved.

In 2007, Zhang *et al.* [21] irradiated As_2S_3 glass with a femtosecond laser to improve the NLO performance; results showed that n_2 improved by as much as 50%. However, several studies have illustrated that applying high-energy radiation leads to anisotropic nonlinear enhancement[22]; moreover, this method can only achieve a small range of surface doping, which is difficult to use in case of large bulk materials. Nevertheless, the emergence of noble-metal NP-doped glass fibers can organically combine the advantages of glass fibers and noble metal NPs and effectively avoid their respective shortcomings, which makes them promising candidates for fabricating high-performance NLO fibers[7, 19, 23-24]. Moreover, noble-metal NPs, because of their ability to localize and enhance the incident electromagnetic field, have become good candidates as optical nanostructures to improve luminescence performance in case of doped glasses[25]. In 2014, Chen demonstrated that introducing an appropriate amount of Ag^+ into a glass matrix considerably increases $\chi^{(3)}$ from 0.87×10^{-10} to 26.32×10^{-10} esu at an 800 nm wavelength; however, further increasing the content of Ag^+ results in severe particle aggregation owing to the Ostwald ripening process, which is not conducive to glass fiber preparation[19]. Therefore, promoting the nonlinearity of noble-metal NP-doped glass fibers remains challenging.

In this study, phosphate glass with high ion solubility and bismuth glass with unique self-reduction characteristics and high optical nonlinear performance were selected as the glass matrices[26-28], and a highly nonlinear glass with heavy Ag-NP doping in a hybrid phosphate-bismuthate (PB) glass system was ingeniously developed. After calculation, the highest doping amount of Ag was as high as 35%. Moreover, the saturation absorption (SA) and reverse saturation absorption (RSA) were as high as 4.94×10^{-12} and -14×10^{-12} $m\cdot W^{-1}$ at 800 nm, respectively. To elucidate the influence of noble metal NPs and the glass matrix on nonlinear performance, a series of analyses, including Raman spectroscopy, transmission electron microscopy (TEM), and Z-scan measurements, were performed. Results showed that the nonlinearity of PB glass considerably increased because of the formation of numerous Ag NPs. Furthermore, we successfully fabricated heavily Ag NP-doped PB glass fibers with controlled geometrical properties using a modified "molten-core" drawing method, which laid a certain foundation for batch manufacturing in the future[29-33].

2 Experimental setup

2.1 Preparation of glass samples

Glass matrices comprising $x$$Bi_2O_3$-(66-$x$) P_2O_5-30ZnO-4Al_2O_3 (termed as PxB glass, x=1, 6, 11, 16, and 21) were prepared to determine the formation scope and preliminarily characterize the performance. Analytical reagents of Bi_2O_3, P_2O_5, ZnO, and Al_2O_3 were used as raw materials and precisely weighed with a total batch mass of 30 g. First, these raw materials were mixed and ground into powder in an agate mortar and sealed in a dried corundum crucible. Second, the materials were melted in a well-type furnace at 1150 ℃ for 30 min after premelting at 230 ℃. The obtained molten glass was then rapidly poured onto a heated stainless steel plate and annealed in a muffle furnace at 430 ℃ for 2 h. Finally, the samples were cut into 10 mm×10 mm pieces and the offcut was ground into powder for thermal analysis.

For further study, the influence of the content of Ag NPs on the performance of PB glass was investigated. Silver nitrate [y% (y=1, 2, 5, 7.5, 10, 20, 30, 45, 60)] was introduced into the P11B and P16B glasses

during the stage of weighing the raw materials. The doped glasses are referred to as P11B-yAg and P16B-yAg, and the fabrication procedures were similar to those of the aforementioned PB glasses. Subsequently, the precursors were heat-treated at 550 ℃ for different times to generate Ag NPs. Finally, all glass samples were polished for further optical measurements.

2.2 Preparation of fiber samples

To inhibit uncontrolled crystallization during the fiber drawing process, the "molten-core" method was used to fabricate the PB glass fibers. First, a piece of P11B-10Ag glass was cold-processed into a cylindrical glass rod with a length and diameter of ~30 mm and 3.8 mm, respectively. A commercial K9 glass tube (composition 69.13SiO_2-10.75B_2O_3-3.07BaO-10.4Na_2O-6.29K_2O-0.36As_2O_3, length 100 mm, outer diameter 30 mm, and inner diameter 4 mm) was used as the cladding of the fiber. The P11B-10Ag glass rod was inserted into an expanded channel of the K9 glass tube to form the fiber preform. Finally, the preform was drawn into a composite glass fiber on a commercial fiber drawing tower at a temperature of ~930 ℃.

2.3 Characterization

Optical absorption spectra were obtained using a Perkin Elmer Lambda 900 ultraviolet/visible (UV/Vis) spectrophotometer in the wavelength range of 300–1600 nm. Raman spectra were obtained using a Raman spectrometer (Renishaw inVia) equipped with a 532 nm Nd:YAG laser. The X-ray diffraction (XRD) patterns of the glass powder heat-treated at 570 ℃ were obtained using an X-ray diffractometer (Rigaku D/max-IIIA). The morphology and nanostructure of the glass were investigated using high-resolution transmission electron microscopy (HRTEM, JEM-2100, JEOL, Japan), and the lattice parameters were obtained by analyzing the TEM images. The cross-section of the glass fiber was observed via scanning electron microscopy (SEM, Quanta200, Hitachi, Japan), and the elemental distribution at the cross-section was investigated using an electro-probe microanalyzer (EPMA-1600, Shimadzu, Japan).

The open-aperture Z-scan technique was used to investigate the saturable absorption properties of the as-fabricated glasses. The femtosecond laser adopted a Coherent Legend Elite Ti: sapphire regenerative amplifier system, which emitted a laser pulse centered at 800 nm with a repetition rate of 10 kHz and a pulse width of 230 fs. The incident beam was focused by a lens with a focal length of 100 mm, resulting in a beam waist of 42.5 μm, and propagated perpendicularly toward the sample. The sample was set perpendicular to the beam axis at the focal plane, which could move linearly along the laser light. During the test, a dual-detector power meter controlled by a computer was used to simultaneously detect the laser power before and after the glass sample with respect to different Z positions.

3 Experimental results and discussion

3.1 Influence of Bi_2O_3 component on phosphate glass

For noble-metal NP-doped glasses used in optical devices, the thermal properties exert a strong effect on the crystallization behavior during heat treatment. The thermal characterization results for PxB glasses (x=1, 6, 11, and 16, except 21 because P21B glass suffers from severe crystallization and devitrification) are shown in Fig. 1(a). As can be seen in this figure, the glass transition temperature (T_g) decreases with increasing Bi_2O_3: P_2O_5 ratio and the crystallization temperature of P16B is ~571 ℃. Thus, the XRD spectra of the PxB glasses after heat treatment at 570 ℃ for 2 h can provide additional information regarding the influence of introducing Bi_2O_3 into phosphate glasses. As shown in Fig. 1(b), distinct crystallization peaks attributed to $BiPO_4$ NPs are observed in case of the P16B glass, whereas a broad-hump diffraction band from 20° to 30° is observed in case of the P1B, P6B, and P11B glasses. The presence of distinct crystallization peaks is attributable to the high doping content. indicating that the introduction of Bi_2O_3 into phosphate glass adversely affects the thermal stability of phosphate glass. To gain insight into the effects of Bi_2O_3 on the structure of phosphate glass, the Raman spectra of the PxB glasses are illustrated in Fig. 1(c). The phosphate units transform from highly aggregated $(PO_3)^-$ units to dispersed $(P_2O_7)^{4-}$ units with increasing Bi_2O_3 content[34-35]. The disaggregation of phosphate units is caused by an increasing amount of nonbridged oxygen, which originates from the network-breaking effect of [BiO_6] units.

The localized surface plasmon resonance (LSPR) bands of the PxB glasses with different contents of Bi_2O_3 were measured; these bands are shown in Fig. 1(d). The Bi NPs embedded in the glass matrix can be determined on the basis of the LSPR band located at ~460 nm[23, 36]. The LSPR band appears and shifts gradually toward a longer wavelength with increasing Bi_2O_3 content. An increase in the number of Bi NPs is attributable to the enhancement of the LSPR band intensity. The distinct red-shift of the LSPR band confirms the aggregation and growth of Bi NPs. To illustrate this phenomenon,

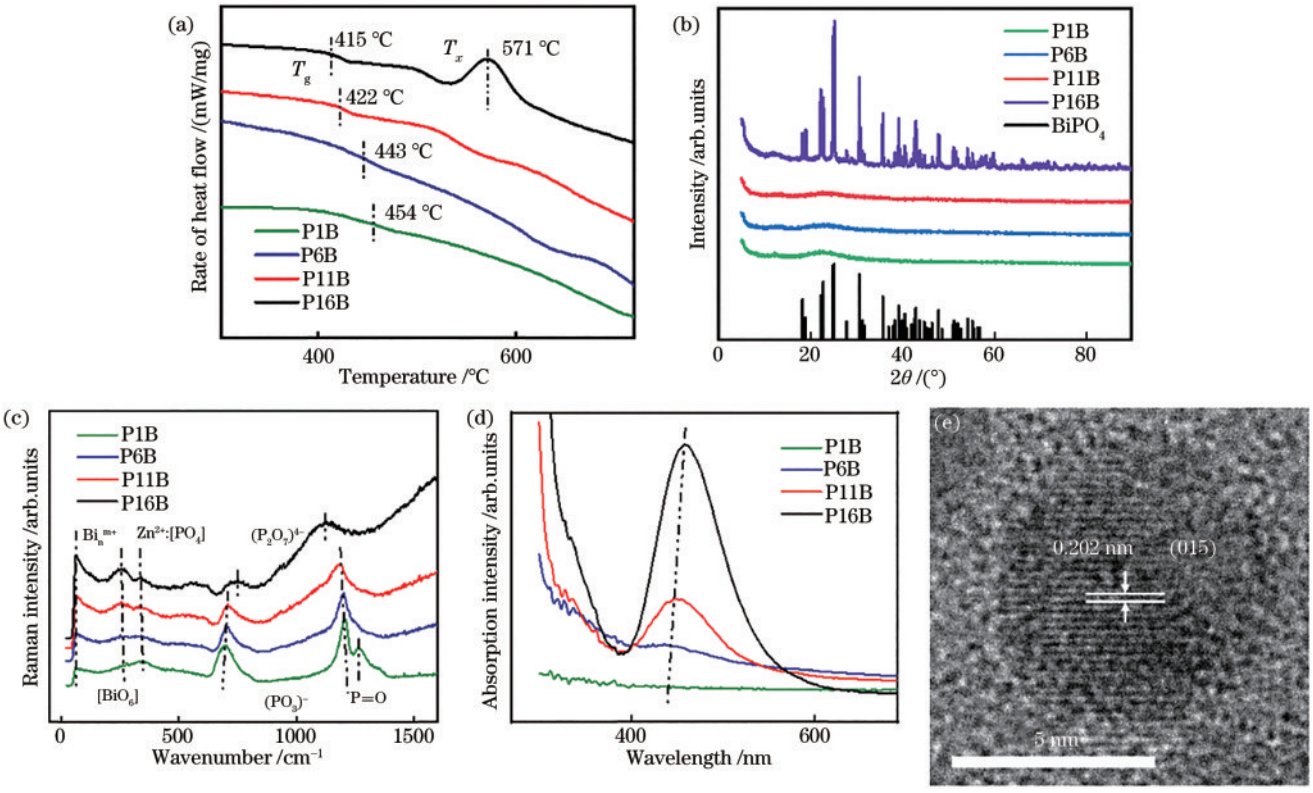

Fig. 1 Characterization of PxB matrix glass. (a) Thermal analysis curves of PxB glasses with noted transforming temperature (T_g) and crystallizing temperature (T_x); (b) XRD spectra of PxB glasses annealed at 570 ℃; (c) Raman and (d) absorption spectra of PxB glasses; (e) HRTEM image of one Bi nanoparticle (Bi-NP) in the PB glass

the HRTEM image of the P16B glass is shown in Fig. 1(e). The observation of Bi NPs in the image verifies the aforementioned phenomenon. Reportedly, the bismuthate component in glass at high temperatures exhibits a trend of self-reduction from Bi^{3+} to Bi^{2+}, Bi^{+}, Bi^{0}, or ions with lower valence states[37-39], which may be conducive to the reduction and formation of Ag NPs in PxB glass. The aforementioned results confirm that appropriate doping with Bi_2O_3 enhances the LSPR band intensity, whereas excessive Bi_2O_3 doping results in poor thermal stability of PxB glass, which is unconducive to optical fiber fabrication.

3.2 Formation of Ag NPs in PB glass

The LSPR spectra of the Ag NP-doped P11B glass are shown in Fig. 2 (a). Three stages can be observed with increasing Ag content. First, the intensity of the LSPR band at ~445 nm of Bi NPs gradually decreases and then disappears in case of the P11B-2Ag glass, indicating that Bi NPs are oxidized into high valence states when introducing Ag^{+} ions. Second, the LSPR band at ~425 nm assigned to Ag NPs appears and its intensity reaches the optimum in case of the P11B-7.5Ag glass. However, the LSPR band suddenly disappears by further increasing the Ag^{+}

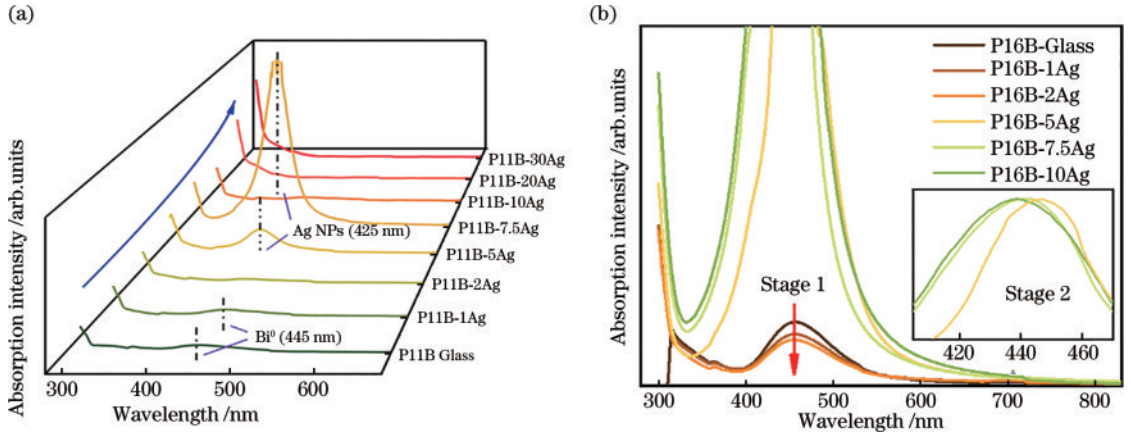

Fig. 2 Spectra. (a) Optical absorption spectra of the glass samples containing $x$$Al_2O_3$ (x = 0–13%); (b) contour plot of the emission-excitation map from the 6Al glass sample

content, indicating that the content of Ag NPs decreases rapidly. A similar variation, but without the final stage of the LSPR band, can also be observed in case of the P16B-*y*Ag glass, as shown in Fig. 2(b). The variation in the LSPR intensity is attributable to the oxidation of low-valence bismuth ions, rather than an increase in the number of Ag NPs. However, a slight blue-shift of LSPR peaks observed in the inset of Fig. 2(b) can be attributed to a morphological variation, which results from the formation of elliptical NPs.

To gain insight into the formation of Ag NPs in the P11B-yAg and P16B-yAg glasses, the TEM and HRTEM images of the Ag NPs in the P11B and P16B glasses were obtained; these images are shown in Fig. 3. As shown in Figs. 3(a), (c), and (e), spherical and nonspherical Ag NPs coexist and are uniformly dispersed in the glass matrices. The statistical diameter of the NPs was measured using the scale depicted in the inset. Based on the Gaussian fit, the average diameters were determined to be 20.5 nm and 21.6 nm for the P11B-7.5Ag and P11B-30Ag samples, respectively.

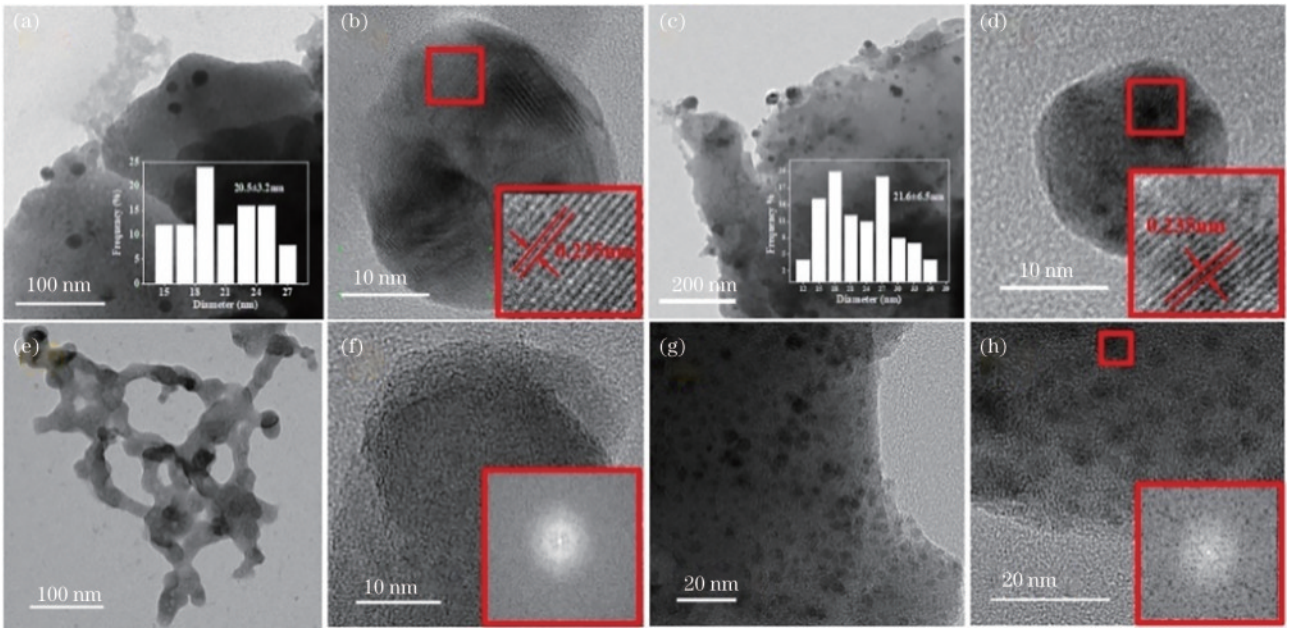

Fig. 3 Micro-morphologies of nanoparticles and nanoclusters in glass. TEM images of (a) P11B-7.5Ag glass, (c) P11B-30Ag, (e) P11B-60Ag, and (g) P16B-7.5Ag. HRTEM of single Ag-NP (b) single Ag-NP in P11B-7.5Ag (inset: crystal plane), (d) single Ag-NP in P11B-30Ag glass (inset: crystal plane), (f) single amorphous particle in P11B-60Ag glass (inset: electron diffraction pattern), and (h) feature of P16B-7.5Ag glass (inset: electron diffraction pattern)

However, the Ag NPs in the glass samples differ in certain aspects. With increasing Ag^+ content, the morphological state of Ag NPs gradually changes from intact to amorphous [Figs. 3(b), (d), and (f)]. This can be reasonably attributed to partial aggregation caused by the Ostwald ripening process owing to the presence of high Ag^+ content in P11B-30/60Ag. Particles with various shapes are observed, and their long electron mean free paths cause a weak confinement effect, thereby resulting in a considerably broad but weak SPR absorption band[19]. We assume that the formation of Ag clusters generated by excess Ag^+ disrupts the conditions for generating plasma resonance, thereby leading to the disappearance of the LSPR peak, which can explain the abnormal phenomenon that no distinct LSPR band is observed in case of the P11B glass with heavy Ag^+ doping. Unlike the Ag NPs in the P11B-7.5Ag glass, although the Ag NPs in the P16B-7.5Ag glass are uniformly dispersed, as shown in Fig. 3(g), the electron diffraction pattern [Fig. 3(h)] presents an amorphous state of the particles in the glass, indicating that the high Bi content in the phosphate glass inhibits the precipitation of Ag NPs. A reasonable explanation for this phenomenon can be described as follows: an increase in Bi^{3+} content in the glass matrix reduces the rigidness of the glass network [Fig. 1(c)] because the size mismatch between Bi^{3+} and other small forming glass cations (including P^{5+} and Al^{3+}) is enhanced. However, the loose network of heavily Bi_2O_3-doped glass allows Ag^+ to move freely in the glass, share valence electrons with additional O^{2-} anions and Ag^0, and form additional glass network terminals, thereby generating additional clusters and reducing the crystallinity of Ag NPs.

3.3 Variation in glass structure of PB glass

To clarify the relationship between crystallization and the glass structure, Raman spectra shown in Fig. 4 are used to analyze the variation in the glass structure. Similar to Fig. 1(c), the transformation from $(PO_3)^-$ units to $(P_2O_7)^{4-}$ units is also observed in both the P11B-*y*Ag and P16B-*y*Ag glasses with increasing Ag^+ content. In addition, the spacing of the marked peaks is close to 310 cm^{-1}, indicating that the glass network approaches the limitation of crystallization, which is referentially significant when estimating the formation range of PB glass. Meanwhile, the peaks of $[BiO_6]$ and other units barely change, which indicates the depolymerization of the glass networks and an increase in the amount of non-bridging oxygen, decreasing the number of Bi NPs[40-41]. During the variation in the glass structure during melting[42], Ag NPs and clusters are formed according to the following chemical equation:

$$3Ag^+ + Bi^0 = Bi^{3+} + 3Ag^0, \quad (1)$$

$$nAg^0 = Ag\ NPs, \quad (2)$$

$$mAg^0 + nAg^+ = Ag_m^{n+}。 \quad (3)$$

These equations explain the variation in the valence state of the Ag composition in the three periods shown in Fig. 2(a). First, introducing Ag^+ into the glass triggers the reaction in Equation 1, which results in the decrease of Bi^0 and formation of Ag^0. Second, the Ag^0 content reaches a threshold, and the reaction in Eq. (2) occurs when the glass is annealed at 550 ℃, resulting in the formation of Ag NPs. Finally, the Ag^0 content exceeds the threshold, and excessive Ag^+ ions prevent Ag^0 from forming NPs, which prevents the reaction in Equation 2 and leads to a new reaction shown in Equation 3. However, an excessive introduction of Ag^+ generates additional non-bridging oxygen in the glass network, which disintegrates the glass network and oxidizes low-valence Bi^0 into high-valence states[38, 43-44], thereby preventing the progress shown in Equation 1. Therefore, Ag^+ eventually exists as clusters.

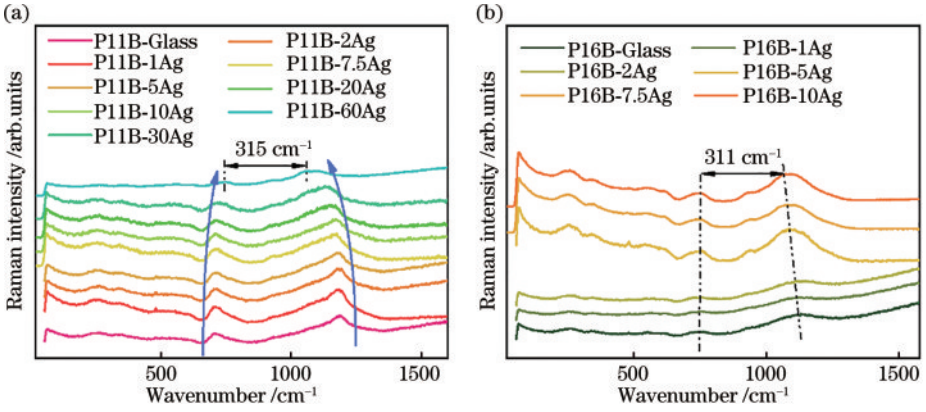

Fig. 4 Raman spectrum. (a) P11B-*y*Ag glass; (b) P16B-*y*Ag glass

To gain a better understanding of the aforementioned phenomenon, we extended the annealing time and compared the LSPR peaks of the Ag-doped glass. As shown in the photographs [Fig. 5(a)] of the glass samples, the color of the glass samples varies with the Ag content and annealing time. The color of the glass gradually deepens as the heat-treatment time increases when the silver nitrate mass fraction does not exceed 45%. The glass samples are almost colorless when silver nitrate mass fraction exceeds 45%. Moreover, similar absorption bands (~445 nm) attributed to the Bi NPs [Fig. 5(b)] indicate that the content of Bi^0 in the glass is barely affected by different annealing times for a small amount of Ag^+.

Consistent with the color variation in Fig. 5(a), the intensity of the LSPR bands at ~425 nm assigned to Ag NPs increases with increasing annealing period [Figs. 5(c)-(e)], indicating that Ag NPs are considerably affected by the annealing time. Notably, Fig. 5(e) shows that the slope between 320 nm and 380 nm, which is regarded as the absorption of Ag nanoclusters, gradually disappears. This implies that the main aggregation process of Ag^0 changes from Eq. (2) to Eq. (3). As expected, the absorption curves remain unchanged in Figs. 5(f) and (g) without a visible LSPR band, indicating low Bi^0 content during the melting process and that most silver compositions exist as clusters. Thus, we have demonstrated the formation mechanism of Ag NPs in PB glass and summarized it into three chemical equilibria. A high content of Ag NPs has been confirmed to be formed in PB glasses. Using novel methods, it is possible to form considerably larger amounts of Ag NPs in PB glasses.

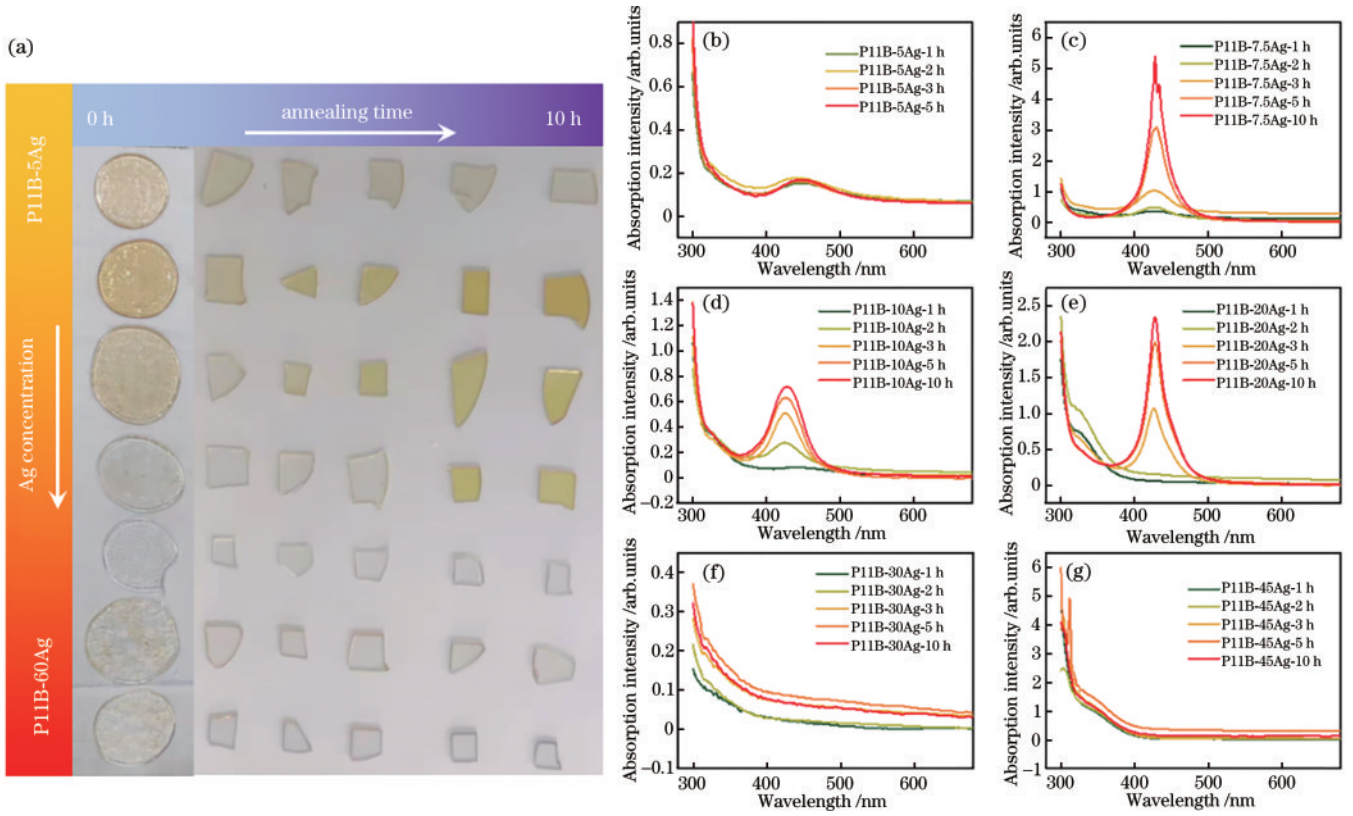

Fig. 5　Picture and absorption spectrum of glass samples with different Ag mass fractions and annealing times. (a) Glass samples of different Ag contents and annealing times; (b)–(g) absorption spectrum of P11B-xAg glasses (x=5, 7.5, 10, 20, 30, 45)

3.4　NLO response of Ag NP-doped PB glass

To further investigate the nonlinear absorption of the P11B-10Ag glass annealed at different times, the open-aperture Z-scan technique with a femtosecond pulsed laser at 800 nm was performed, as shown in Fig. 6. A visible valley appears in the fitting curve, illustrating that two-photon absorption (TPA) dominates the main absorption process. The normalized transmittance can be described as follows:

$$T(z)=1-\beta I_0 L_{\mathrm{eff}}/2\sqrt{2}\,(1+z^2/z_0{}^2), \qquad (4)$$

where β denotes the third-order nonlinear absorption coefficient, I_0 and z_0 denote the peak intensity of the laser and Rayleigh range at the focus (z=0), respectively, L_{eff} denotes the effective thickness of the glass sample. β can be calculated by fitting the experimental data, and after calculation, the β value of the P11B-10Ag glass is as high as 4.9×10^{-12} m·W^{-1} after annealing for 24 h, which is 40 times larger than that of short-term annealing. Compared with previously reported NLO materials[19], the glass sample exhibits excellent RSA, which promises great potential in the applications of NLO fibers and devices.

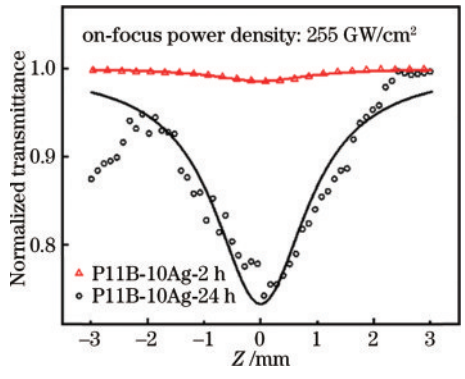

Fig. 6　OA Z-scan measurements of P11B-10Ag glass annealed for 2 h and 24 h, respectively

Unlike the P11B-10Ag glass, long-term annealing results in an unexpected influence on the LSPR peak in the absorption spectra of the P16B-10Ag glass. As shown in Fig. 7(a), the profile of the LSPR band became broad and asymmetric and a new broad absorption band appeared at ~800 nm after annealing for 12 h. The noticeable shift and asymmetry confirm the formation of Ag NPs, particularly the morphological variation, including the formation of elliptical NPs and their aggregation and growth after long-term annealing. The Z-scan measurements of the P16B-10Ag glass at 800 nm also support this conclusion. Long term-annealed samples exhibit saturable absorption, whereas short term-annealed samples exhibit RSA. The reversal of RSA confirms the growth of Ag NPs. The results and fitting curve of the Z-scan measurements

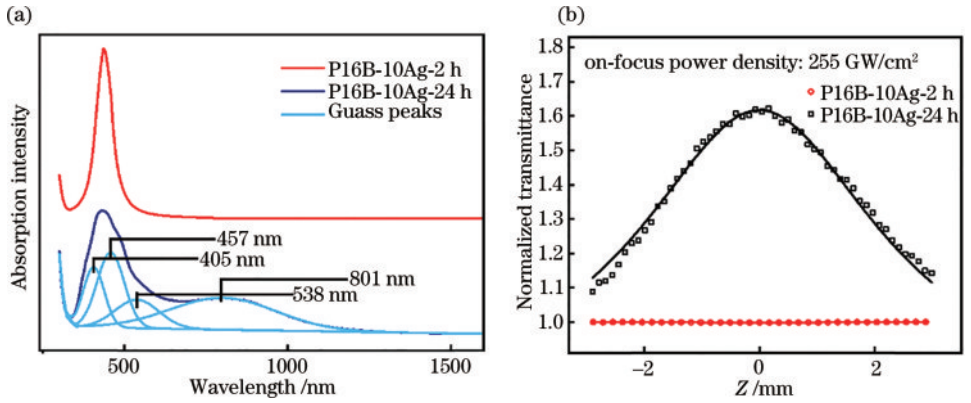

Fig. 7 (a) Absorption spectrum and (b) OA Z-scan result of P16B-10Ag glass annealed for 2 h and 24 h

are shown in Fig. 7 (b). The calculated nonlinear absorption coefficient β is increased from 1.4×10^{-14} to -14×10^{-12} m·W^{-1}, which is higher than that of many other SA materials[42, 45-46].

3.5 Fiber drawing of Ag NP-doped PB glass

The "molten-core" method is used to fabricate PB glass fibers with heavy Ag-NP doping. The fiber preform is prepared by inserting a P11B-10Ag glass rod into a K9 glass tube [Fig. 8(a)]. After the drawing process, a glass fiber with a distinct core-cladding boundary is obtained. Both the cross-section shape and the core-cladding ratio conform to the geometrical characteristics of the precursor considerably well [Fig. 8(b)]. The elemental distribution map at the cross-section of the fiber indicates that the basic glass compositions of the fiber core are adequately constrained, including Al, P, Zn, Bi, and Si. However, in addition to dispersing in the fiber core, Ag diffuses into the cladding and preferentially accumulates in the area neighboring the core rim [Fig. 8(c)]. The SEM and TEM tests show that the particle size of the Ag NPs diffused into the cladding (average: ~7.8 nm) is slightly larger than that of the Ag NPs constrained in the core region (average: ~6.3 nm), as shown in Figs. 8(d)-(f). We speculate that the origin of this distribution phenomenon of Ag NPs is related to the interface-related rheological behavior of the glass melt during the fiber drawing process. The successful fabrication

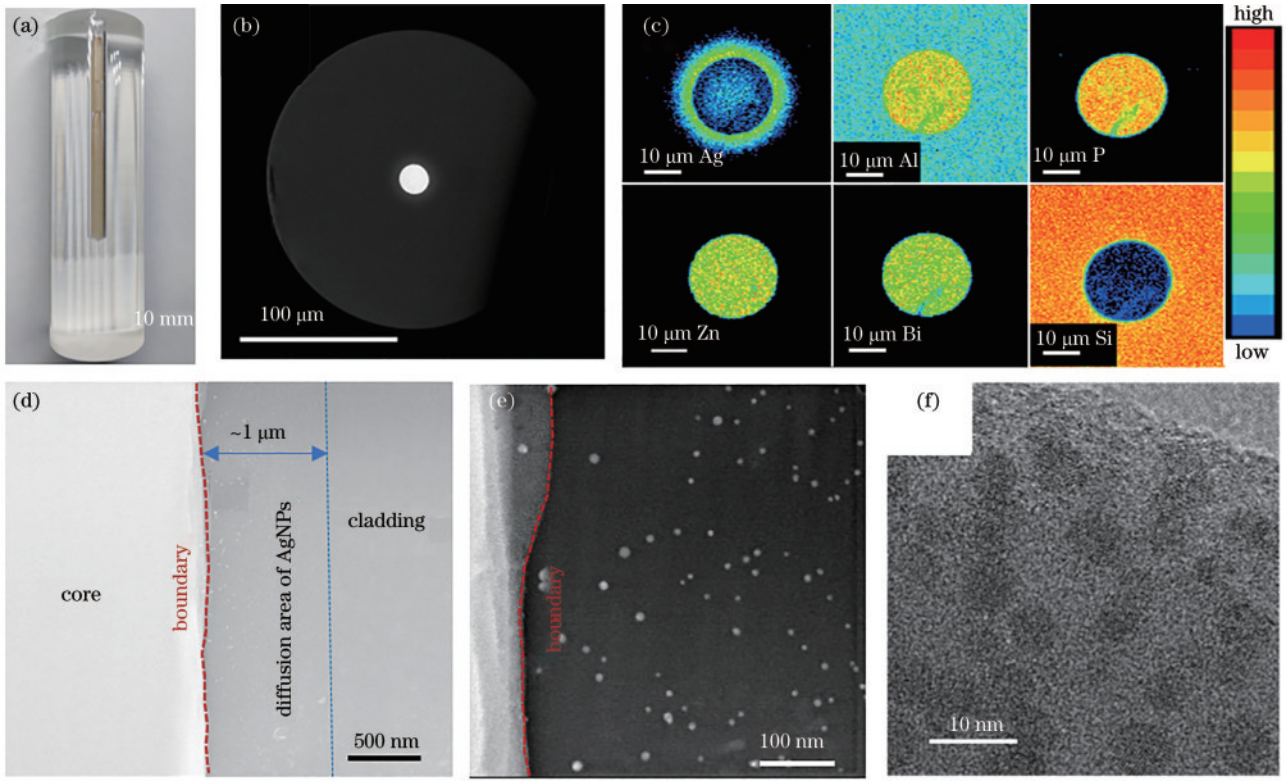

Fig. 8 (a) A digital-camera photo of the fiber preform; (b) an SEM image of the cross section of the Ag-NPs doped PB glass fiber; (c) area elemental distribution map at the cross section of the glass fiber (gathered by EPMA); TEM images of the Ag-NPs doped PB fiber collected at (d) (e) boundary area and (f) central area of the core

of Ag NP-doped glass fiber shows considerable potential for application in the field of NLO devices.

4 Conclusion

In summary, ultrahigh- content Ag NP-doped PB glass has been prepared using a melt quenching method. For the first time, Ag NPs with mass fraction higher than 13% in highly stable glass are reported. To clarify the formation mechanism of Ag NPs, we have investigated the influence of the glass network, nanostructure, and optical properties of the PB glass. The valence state of Ag ions in the glass matrix is demonstrated to be related to the chemical composition of the matrix glass, the content of Ag dopants, and the heat treatment process. After tailoring the composition and fabrication technique, considerable third-order nonlinear effects in the glass samples are achieved. The Ag NP-doped PB glass exhibits strong TPA and SA at 800 nm, and the nonlinear absorption coefficients β reach 4.94×10^{-12} m·W^{-1} and -14×10^{-12} m·W^{-1}, respectively. Overall, the PB glass embedded with a high content of Ag NPs has a simple preparation process, low infrared-band loss, high third-order nonlinear absorption, and excellent thermal stability, making it a promising candidate in applications of optical limiting and ultrafast laser pulses. Finally, we demonstrate that Ag NP-doped PB glass fiber with controlled geometrical properties can be prepared using a "molten-core" fiber drawing method.

Reference

[1] Chai T, Li X H, Feng T C, et al. Few-layer bismuthene for ultrashort pulse generation in a dissipative system based on an evanescent field[J]. Nanoscale, 2018, 10(37): 17617-17622.

[2] Chen B H, Zhang X Y, Wu K, et al. *Q*-switched fiber laser based on transition metal dichalcogenides MoS_2, $MoSe_2$, WS_2, and WSe_2[J]. Optics Express, 2015, 23(20): 26723-26737.

[3] Du J, Zhang M, Guo Z, et al. Phosphorene quantum dot saturable absorbers for ultrafast fiber lasers[J]. Scientific Reports, 2017, 7: 42357.

[4] Guo B, Xiao Q L, Wang S H, et al. 2D layered materials: synthesis, nonlinear optical properties, and device applications[J]. Laser & Photonics Reviews, 2019, 13(12): 1800327.

[5] Koulouklidis A D, Gollner C, Shumakova V, et al. Observation of extremely efficient terahertz generation from mid-infrared two-color laser filaments[J]. Nature Communications, 2020, 11: 292.

[6] Liu W J, Liu M L, Chen X, et al. Ultrafast photonics of two dimensional $AuTe_2Se_{4/3}$ in fiber lasers[J]. Communications Physics, 2020, 3: 15.

[7] Nie W J, Zhang Y X, Yu H H, et al. Plasmonic nanoparticles embedded in single crystals synthesized by gold ion implantation for enhanced optical nonlinearity and efficient *Q*-switched lasing[J]. Nanoscale, 2018, 10(9): 4228-4236.

[8] Rashidian M, Dorranian D. Investigation of optical limiting in nanometals[J]. Reviews on Advanced Materials Science, 2015, 40(2): 110-126.

[9] Wei D Z, Wang C W, Wang H J, et al. Experimental demonstration of a three-dimensional lithium niobate nonlinear photonic crystal[J]. Nature Photonics, 2018, 12(10): 596-600.

[10] Xu J L, Li X Y, Xiong J B, et al. Halide perovskites for nonlinear optics[J]. Advanced Materials, 2020, 32(3): 1806736.

[11] Yamashita S. A tutorial on nonlinear photonic applications of carbon nanotube and graphene[J]. Journal of Lightwave Technology, 2012, 30(4): 427-447.

[12] Yamashita S. Nonlinear optics in carbon nanotube, graphene, and related 2D materials[J]. APL Photonics, 2019, 4(3): 034301.

[13] Zhang M, Wu Q, Zhang F, et al. 2D black phosphorus saturable absorbers for ultrafast photonics[J]. Advanced Optical Materials, 2019, 7(1): 1800224.

[14] Zheng J, Yang W M, Wang J Y, et al. An ultranarrow SPR linewidth in the UV region for plasmonic sensing[J]. Nanoscale, 2019, 11(9): 4061-4066.

[15] Lü Q H, Ma R, Xiao S Y, et al. Principles and applications for optical nonlinear activation function devices[J]. Acta Optica Sinica, 2023, 43(16): 1623001.

[16] Qiao B J, Chen F F, Huang Y C, et al. Investigation of mid-infrared optical nonlinearity of $Ge_{20}Sn_xSe_{80-x}$ ternary chalcogenide glasses[J]. Materials Letters, 2016, 162: 17-19.

[17] Qiu J H, Yang A P, Zhang M J, et al. Ga_2S_3-Sb_2S_3-CsI chalcohalide glasses for mid-infrared applications[J]. Journal of the American Ceramic Society, 2017, 100(11): 5107-5112.

[18] Sugimoto N, Kanbara H, Fujiwara S, et al. Third-order optical nonlinearities and their ultrafast response in Bi_2O_3-B_2O_3-SiO_2 glasses[J]. Journal of the Optical Society of America B, 1999, 16(11): 1904-1908.

[19] Chen F F, Cheng J W, Dai S X, et al. Third-order optical nonlinearity at 800 and 1300 nm in bismuthate glasses doped with silver nanoparticles[J]. Optics Express, 2014, 22(11): 13438-13447.

[20] Wu C F, Pan H, Zhu Y C. Electric field enhancement for hybrid structure containing silver grating and silver nanoparticles[J]. Chinese Journal of Lasers, 2022, 49(6): 0608003.

[21] Zhang Q M, Liu W, Liu L Y, et al. Large and opposite changes of the third-order optical nonlinearities of chalcogenide glasses by femtosecond and continuous-wave laser irradiation[J]. Applied Physics Letters, 2007, 91(18): 181917.

[22] Xiang H, Wang S F, Wang Z W, et al. Laser irradiation

induced enhancement on the ultrafast third-order optical nonlinearity of chalcogenide glass[J]. Optical Materials, 2006, 28(8/9): 1020-1024.

[23] Fang Y Z, Meng S H, Hou J S, et al. Experimental study of growth of silver nanoparticles embedded in Bi_2O_3-SiO_2-B_2O_3 glass[J]. Journal of Alloys and Compounds, 2019, 809: 151725.

[24] Zhao Y Y, Dong N N, Qiu P P, et al. The nonlinear optical properties of silver nanoparticles decorated glass obtained from sintering mesoporous powders[J]. Journal of the American Ceramic Society, 2021, 104(6): 2571-2578.

[25] Wei R F, Li J J, Gao J Y, et al. Enhancement of Eu^{3+} luminescence by Ag species (Ag NPs, ML-Ag, Ag^{+}) in oxyfluoride glasses[J]. Journal of the American Ceramic Society, 2012, 95(11): 3380-3382.

[26] Nelson C, Tallant D R. Raman studies of sodium phosphates with low silica contents[J]. Physics and Chemistry of Glasses, 1985, 26(4): 119-122.

[27] Ardelean I, Cora S, Ioncu V. Structural investigation of CuO-Bi_2O_3-B_2O_3 glasses by FT-IR, Raman and UVNIS spectroscopies[J]. Journal of Optoelectronics and Advanced Materials, 2006, 8(5): 1843-1847.

[28] Bingham P A, Hand R J, Hannant O M, et al. Effects of modifier additions on the thermal properties, chemical durability, oxidation state and structure of iron phosphate glasses[J]. Journal of Non-Crystalline Solids, 2009, 355(28/29/30): 1526-1538.

[29] Morris S, Ballato J. Molten-core fabrication of novel optical fibers[J]. American Ceramic Society Bulletin, 2013, 92(4): 24-29.

[30] Fang Z J, Zheng S P, Peng W C, et al. Ni^{2+} doped glass ceramic fiber fabricated by melt-in-tube method and successive heat treatment[J]. Optics Express, 2015, 23(22): 28258-28263.

[31] Fang Z J, Xiao X S, Wang X, et al. Glass-ceramic optical fiber containing $Ba_2TiSi_2O_8$ nanocrystals for frequency conversion of lasers[J]. Scientific Reports, 2017, 7: 44456.

[32] Kang S L, Fang Z J, Huang X J, et al. Precisely controllable fabrication of Er^{3+}-doped glass ceramic fibers: novel mid-infrared fiber laser materials[J]. Journal of Materials Chemistry C, 2017, 5(18): 4549-4556.

[33] Yang S, Heyl H, Homa D, et al. Powder-in-tube reactive molten-core fabrication of glass-clad BaO-TiO_2-SiO_2 glass-ceramic fibers[J]. Materials, 2020, 13(2): 395.

[34] Zhang Y, Zhu W, Hao Z L, et al. Investigation of the P_2O_5-Bi_2O_3-CaO system: glass forming region, structure, properties[J]. Journal of Non-Crystalline Solids, 2023, 600: 122022.

[35] Rao P S, Rajyasree C, Babu A R, et al. Effect of Bi_2O_3 proportion on physical, structural and electrical properties of zinc bismuth phosphate glasses[J]. Journal of Non-Crystalline Solids, 2011, 357(21): 3585-3591.

[36] Wang T T, Zhao J H, Cao Y H, et al. Optical nonlinear enhancement and dynamics of Bi doped chalcogenide glass films[J]. Acta Optica Sinica, 2023, 43(23): 2319001.

[37] Chen W W, Huang X J, Dong Q, et al. Thermally stable and tunable broadband near-infrared emission from NIR-I to NIR-II in Bi-doped germanate glass for smart light sources[J]. Journal of Materials Chemistry C, 2023, 11(3): 953-962.

[38] Xiong P X, Li Y Y, Peng M Y. Recent advances in super broad infrared luminescence bismuth-doped crystals [J]. iScience, 2020, 23(10): 101578.

[39] Liu X Y, Guo H, Liu Y, et al. Thermal quenching and energy transfer in novel Bi^{3+}/Mn^{2+} co-doped white-emitting borosilicate glasses for UV LEDs[J]. Journal of Materials Chemistry C, 2016, 4(13): 2506-2512.

[40] Xing H B, Su L B, Chen X H, et al. Broadband mid-infrared luminescence of Bi_2Se_3 and doped crystals[J]. Laser Physics, 2014, 24(3): 035701.

[41] Yu P S, Su L B, Zhao H Y, et al. Optical and structural characterization of colored $Bi_4Ge_3O_{12}$ crystals[J]. Journal of Luminescence, 2014, 154: 520-524.

[42] Xu T F, Chen F F, Shen X, et al. Observation of surface plasmon resonance of silver particles and enhanced third-order optical nonlinearities in AgCl doped Bi_2O_3-B_2O_3-SiO_2 ternary glasses[J]. Materials Research Bulletin, 2010, 45(10): 1501-1505.

[43] Chen F G, Wang Y F, Chen W W, et al. Regulating the Bi NIR luminescence behaviours in fluorine and nitrogen co-doped germanate glasses[J]. Materials Advances, 2021, 2(14): 4743-4751.

[44] Chen F G, Chen Z, Qiu J R, et al. Highly efficient, tunable, ultrabroadband NIR photoemission from Bi-doped nitridated germanate glasses toward all-band amplification in optical communication[J]. Chinese Optics Letters, 2023, 21(5): 051601.

[45] Singla S, Achanta V G, Pandey O P, et al. Effect of different stabilizers on dispersion of gold nanoparticles in bismuth borosilicate glass and their intensity dependent nonlinear behaviour[J]. Optical Materials, 2019, 96: 109334.

[46] Zhang Y J, Jin Y, He M L, et al. Optical properties of bimetallic Au-Cu nanocrystals embedded in glass[J]. Materials Research Bulletin, 2018, 98: 94-102.